Journal of
Materials Chemistry A

PAPER

View Article Online
View Journal | View Issue

Check for updates

Cite this: *J. Mater. Chem. A*, 2019, 7, 10552

A two-dimensional ion-pump of a vanadium pentoxide nanofluidic membrane†

Raj Kumar Gogoi, Arindom Bikash Neog, Tukhar Jyoti Konch, Neelam Sarmah and Kalyan Raidongia*

Received 22nd November 2018
Accepted 25th March 2019

DOI: 10.1039/c8ta11233a

rsc.li/materials-a

The reactive surface and layered crystal structure of vanadium pentoxide (V_2O_5) are exploited here to prepare a two-dimensional (2D) ion pump that transports ions against their concentration gradient. The exfoliated layers of V_2O_5 were assembled into membrane form to create ion-channels with excellent nanofluidic transport characteristics. At the surface-charge-governed regime, the flexible and freestanding membrane of V_2O_5 showed a remarkable proton conductivity ($\sim$0.01 S cm^{-1}). The activation energy of proton conductivity (0.066 eV) suggests that the exceptional mobility of H^+ ions (5.2×10^{-3} cm^2 V^{-1} s^{-1}) inside V_2O_5 ion-channels originates from the coordinated hopping of charges between the two-dimensionally arranged water molecules. The transport characteristics of V_2O_5 ion-channels can also be tuned just by tailor-cutting its lamellar membranes into different shapes. While rectangular devices of V_2O_5 membranes exhibit linear *I*–*V* curves, the triangularly cut membranes display a diode-like non-linear *I*–*V* curve. The ionic current rectification in the V_2O_5 triangle was found to originate from a combination of the unipolar conductivity of counter-ions inside the 2D nanochannels and geometrical asymmetry. The 2D ion rectifier of V_2O_5 also pumps ions at the rate of 3.32×10^{-8} amp s^{-1} against a 1000-fold concentration gradient under a fluctuating external potential with zero mean.

Introduction

Channels capable of pumping ions against their concentration gradient at the expense of energy derived from ATP hydrolysis are ubiquitous in biology.[1] They not only help cells to communicate with other cells or external environments but also essential for processes like maintaining cellular ion homeostasis and energy conversion. The outstanding transport properties of biological ion-pumps have also inspired researchers to develop artificial nanochannels capable of producing directional movement of ions because such ion-pumps would be crucial for applications like bio-sensing, bio-purification, seawater desalination, and energy harvesting. So far, most of the experimental and theoretical efforts devoted to creating artificial ion pumps are limited to three-dimensional conical nanopores or artificial protein pumps.[2–7] Here, we have demonstrated that atomically thin 2D channels of a triangular vanadium pentoxide membrane can also pump ions against their concentration gradient in the presence of a fluctuating external potential with zero mean. The reconstructed layered 2D ion-pump displays distinct advantages like facile fabrication and scalability. A large number of 2D materials and their possible functionalized derivatives offer several ways to tune parameters like ionic flux and pumping efficiency. Functionalization of the building blocks could also lead to creation of new functionalities like photo-switchable[8] or temperature-switchable smart ion-pumps. Moreover, the macroscopic dimensions of the nanochannel assemblies overcome the requirement of expensive and sophisticated devices to fabricate devices and offer new opportunities to study the interesting ion transport properties.

Named after the Scandinavian goddess of beauty and fertility, vanadium forms an exceptionally rich variety of oxides that exhibit a range of fascinating properties like metal–insulator transitions, photochromism, thermochromism, and electrochromism.[9–12] These unique properties also provide a platform for the development of many futuristic applications like electrical/optical switching devices, smart windows, and variable reflectance/emittance surfaces.[13–15] Variable oxidation states and the exceptionally active surface of vanadium oxides are also exploited for preparing catalysts for several industrially important chemical processes like manufacturing of sulfuric acid, synthesis of phthalic anhydride, and reduction of nitrogen oxides from the flue gas of power plants.[16] Likewise, tremendous amounts of research efforts are being devoted to exploit the layered-crystal structure and high specific capacity of vanadium oxides to prepare electrode materials for energy storage technologies like lithium/sodium/zinc ion batteries and supercapacitors.[17–20] However, the active surface and

---

Department of Chemistry, Indian Institute of Technology Guwahati, Guwahati, 781039, Assam, India. E-mail: k.raidongia@iitg.ac.in

† Electronic supplementary information (ESI) available: Materials, methods, characterization, fabrication of devices and Fig. S1–S12 and Table S1. See DOI: 10.1039/c8ta11233a

infinitesimally thin space between the layers of vanadium oxides are not yet explored to prepare nanofluidic channels to study ionic/molecular transport behaviours under extreme size-confinement. The molecularly thin nanofluidic channel between the layers of reconstructed layered materials has been already shown to exhibit a rich collection of exciting nanofluidic properties,[21,22] and also promises technological breakthroughs in the areas like molecular sieving,[23] manipulation of single molecules[24,25] and energy harvesting.[26–31] For example, nanofluidic membranes prepared from layered graphene hydrogels and kaolinite-based Janus nanobuilding blocks were employed to harvest energy through pressure driven electrokinetic ion transportation,[29,31] and the cascading lamellar nanochannels of oppositely charged graphene oxide membranes were used for reverse electrodialysis based osmotic power generation.[30] With the unique optical and electronic properties intrinsically associated with their sheets, molecularly thin nanofluidic channels of vanadium oxides could offer a new platform for discovering exciting new nanofluidic and mixed conducting properties. Moreover, systematic studies on the ion transport characteristic through the interlayer space of vanadium oxides would help to understand/improve their performance in areas like lithium/sodium ion batteries, chemical sensing, and catalysis.

Among the different oxides of vanadium, V_2O_5 is taken here as the model system mainly because of its high stability, abundance, and ease of synthesis.[18,32,33] V_2O_5 crystallizes into an orthorhombic (*Pmmn*) layered structure, where each layer can be described as a sheet of square pyramids that share edges and corners. The adjacent layers are stacked *via* weak van der Waals interactions, and the space between the stacked layers allows movement of molecules and/or ions. In the process of materializing the potential applications of V_2O_5, like in supercapacitors, lithium/sodium ion batteries, catalysis, and chemical sensing, detailed understanding of the transport characteristics of intercalating ions and molecules could play a decisive role.

Results and discussion

In the present study, nanosheets of V_2O_5 were exfoliated from bulk V_2O_5 powder by treating them with H_2O_2 under ice cold conditions, inspired by a method already existing in the literature.[19] As can be seen from the digital photo in Fig. 1a, the brown coloured product obtained from the reaction of V_2O_5 and H_2O_2 forms a stable dispersion in water. The dispersion shown in Fig. 1a, having a concentration of 3 mg ml^{-1}, was kept undisturbed for 3 months. By Transmission Electron Microscopy (TEM) investigation, the aqueous dispersion of the V_2O_5 sample displayed a large number of 2D sheets with dimensions in the range of 100 to 400 nm; a representative image of the same is shown in Fig. 1b. The exfoliation of the bulk crystals into atomically thin 2D sheets was further confirmed by analysing the sample under an Atomic Force Microscope (AFM), which also revealed the thicknesses of the sheets to be in the range of 3 to 9 nm. A typical AFM image along with the height profile of V_2O_5 sheets is shown in Fig. 1c and ESI Fig. S1.† The zeta potential of the V_2O_5 dispersion was measured to be -56 ± 1.3 mV, suggesting that the surface of the nanosheets is composed of negative charges, originating from the water assisted dissociation of V–OH groups. Existence of –OH groups

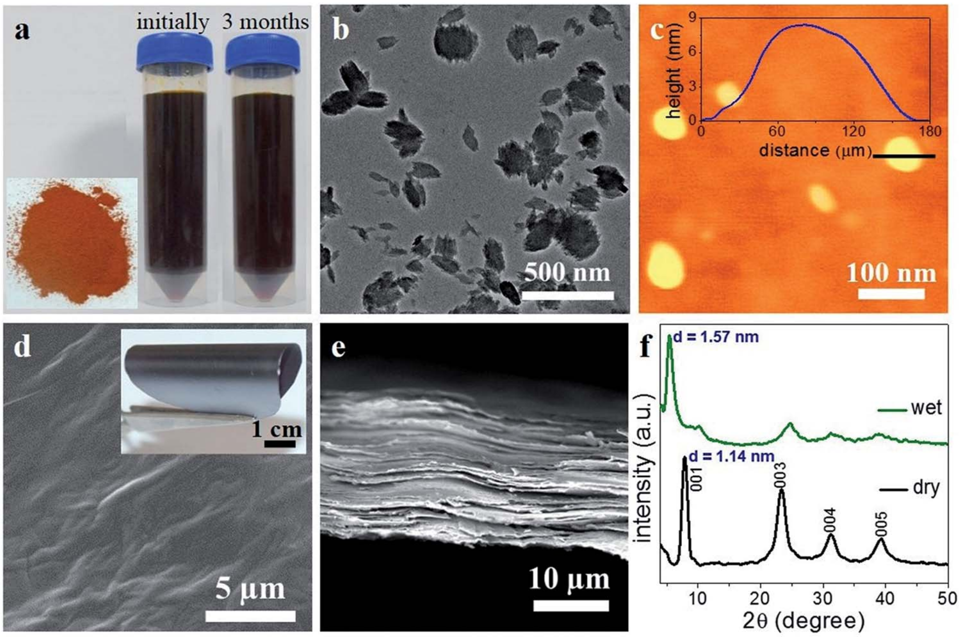

Fig. 1 Freestanding and flexible membrane of V_2O_5: (a) digital photos of an aqueous dispersion of V_2O_5 nanoflakes, stable up to 3 months, obtained by the reaction of bulk V_2O_5 powder (shown in the inset) with H_2O_2 under ice cold conditions. (b) TEM and (c) AFM images along with the corresponding height profile of V_2O_5 nanosheets. FESEM images showing (d) the outer surface, and (e) cross-section of the freestanding membrane prepared by self-assembling V_2O_5 nanosheets. A photo of the flexible V_2O_5 membrane is shown in the inset of (d). (f) XRD pattern of the as-prepared V_2O_5 membrane under dry and wet conditions.

on the exfoliated V_2O_5 sample was also indicated by infrared spectroscopic analysis, as shown in ESI Fig. S2.† The high solution stability of the V_2O_5 nanosheets is attributed to small sheet dimensions and high zeta potential.

In order to create ultra-confined spaces between the nanosheets, an aqueous dispersion (3 mg ml^{-1}) of exfoliated V_2O_5 was vacuum filtered through a PTFE filtration membrane. During the filtration process, due to its large aspect ratio (~45), nanosheets of V_2O_5 were self-assembled in a lamellar fashion forming a macroscopic film on top of the PTFE membrane. The film got detached from the filtration membrane upon air-drying under ambient conditions. A digital photo of the as-prepared flexible and free-standing membrane of V_2O_5 is shown in the inset of Fig. 1d. The thickness of the as-prepared V_2O_5 membrane can be easily tuned by changing the volume and concentration of the dispersion used in the filtration process. The smooth surface (Fig. 1d) and lamellar cross-section (Fig. 1e) of the V_2O_5 membrane were clearly revealed by Field Emission Scanning Electron Microscopy (FESEM) examination. The periodic stacking of the sheets was also confirmed by the sharp XRD reflection at ~1.14 nm, which corresponds to the interlayer spacing of V_2O_5 sheets in the "*c*" direction (001 plane),[19,34] refer to the XRD pattern shown in Fig. 1f. To study the stability of the membranes in water, a rectangular strip (dimensions, 18 mm × 6 mm) of the membrane was soaked in water for a prolonged time. As seen in ESI Fig. S3,† the membrane remained unaltered even after five days. This water stability of the V_2O_5 membranes is attributed to factors such as van der Waals interactions, H-bonding and crosslinking of the flakes by trace amounts of multivalent vanadium cations (like V^{3+}, V^{2+} and VO^{2+}) etched out during the exfoliation process. When soaked in water, the channels of the V_2O_5 membrane are hydrated, and the interlayer spacing between the sheets increases from 1.14 nm to 1.57 nm (Fig. 1f). Considering the thickness of a single V_2O_5 layer as 0.28 nm,[35] the space available for the ion/molecular movement between the sheets is estimated to be around 1.29 nm. In order to obtain further insight into the layer spacing, an aqueous solution (500 ppm, 20 ml) of methylene blue dye (size ~ 1.7 nm) was filtered through a V_2O_5 membrane. As shown in the ESI (Fig. S4†), the V_2O_5 membrane (weight 15 mg) separated up to 10 mg of the dye. In comparison, when a V_2O_5 membrane is directly soaked in a similar dye solution, it could absorb just 1 mg of dye molecules, suggesting the size exclusion limit of the V_2O_5 membrane is smaller than the size of methylene blue molecules.

In order to study the ion transport characteristics of the infinitesimally small space between the V_2O_5 sheets, nanofluidic devices were prepared by cutting the freestanding membranes (thickness 42 μm) into rectangular pieces with dimensions of 18 mm × 4 mm and embedding the same into a freshly prepared PDMS elastomer. After curing the elastomer, two reservoirs of about 0.3 ml in volume were carved out to bring the ends of the V_2O_5 strip in contact with the desired liquids, see Fig. 2a. After hydrating the nanochannels by soaking the devices in water for 24 hours, the reservoirs were filled with electrolyte solutions of required concentrations and left undisturbed for 6 hours to reach the equilibrium. Finally, two Ag/AgCl electrodes connected to a source meter instrument (Keithley 2450) were inserted into the reservoirs to measure the ionic current through the reconstructed V_2O_5 membrane. Fig. 2b shows the current–voltage (*I*–*V*) curves recorded through the V_2O_5 nanofluidic devices with different KCl concentrations. The linearity of the *I*–*V* curve confirms the formation of a continuous network of hydrated channels through V_2O_5 nanosheets. The conductance of the nanofluidic devices obtained from the slope of the *I*–*V* curves was normalized with the overall membrane dimensions, that is the length (*l*), width (*w*), and thickness (*t*) of the rectangular pieces, to calculate the nanofluidic ionic conductivity. In Fig. 2c, conductivity values calculated for the V_2O_5 membrane are plotted as a function of salt concentration. As typical nanofluidic devices, freestanding V_2O_5 membranes show the characteristics of surface-charge-governed ionic conductivity. In the high concentration regime (0.1 to 1 M), the conductivity of the nanochannels resembled that of bulk solutions, but in the low concentration regime (10^{-1} to 10^{-6} M), it did not change even for five orders of magnitude change in the electrolyte concentrations. The surface-charge-governed ionic conductivity indicates overlapping of the Debye lengths of the channel surfaces, and hence the concentration inside the nanochannels is determined by the surface charge density of walls and not by the concentration of the reservoirs. In this concentration regime, only the counter-ions are allowed to enter the nanochannels, whereas all the co-ions are rejected. This not only confirms successful construction of a nanofluidic device of V_2O_5 sheets but also suggests the absence of large interconnected macro-pores in the flexible freestanding V_2O_5 membranes. The surface-charge-governed ionic conductivity of V_2O_5 membranes was also observed with aqueous solutions of NaCl and LiCl, as shown in ESI Fig. S5.†

Similar measurements were also repeated with HCl solutions, and conductivity values calculated for different concentrations (10^{-6} to 1 M) of HCl are plotted in Fig. 2d. Similar to KCl solutions, V_2O_5 nanofluidic devices displayed typical surface-charge-governed ionic conductivity with HCl; however, the conductivity values in the surface-charge-governed regime were found to be 3 times higher than that of the KCl solution. To the best of our knowledge, the conductivity of protons in the V_2O_5 membrane, 0.012 ± 0.008 S cm^{-1}, a mean of 12 measurements of 8 different membranes, is among the highest proton conductivity values reported for layered material based nanofluidic devices.[36–39] In order to obtain further insight into the ion selectivity of the V_2O_5 membrane, the transference number of the cation was calculated from the membrane potential (shown in ESI Fig. S7†), determined from the different concentration gradients across the same. The details of this experiment are provided in the ESI (Fig. S7†). In the low concentration regime, for a 100-fold concentration difference (10^{-3} and 10^{-5} M HCl), the transference number of cations was calculated to be 0.97. However, the transference number was decreased to 0.86, when concentrations of HCl were increased to 1 and 10^{-3} M.

The V_2O_5 nanosheets also exhibit intrinsic electrical conductivity, which could have a contribution to the overall conductivity of the nanofluidic channels. In order to separate the possible contribution of electrical conductivity, the conductivity of a V_2O_5

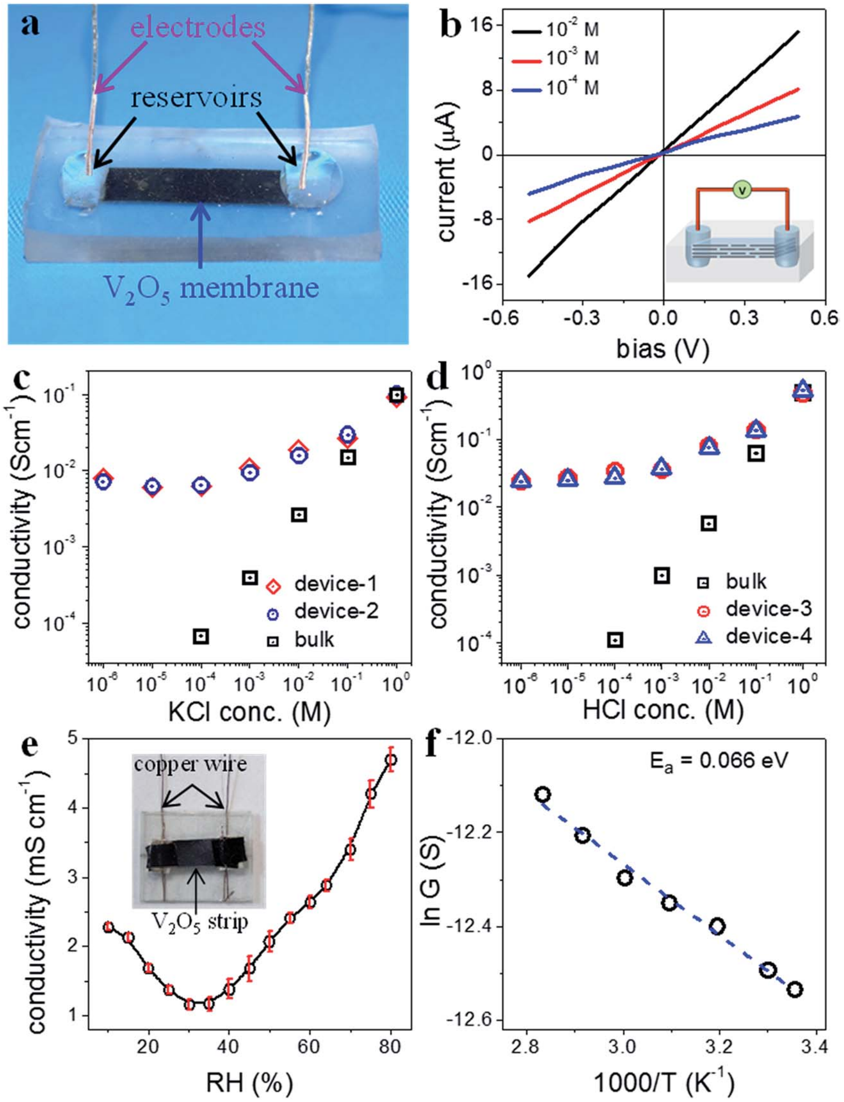

Fig. 2 V_2O_5 based nanofluidic devices: (a) digital photo of a nanofluidic device constructed from the V_2O_5 membrane. (b) *I*–*V* curves, and (c) ionic conductivity of V_2O_5 nanofluidic devices with different KCl concentrations. (d) Proton conductivities as a function of HCl concentration. (e) Humidity dependent conductivity of the V_2O_5 membrane (f) Arrhenius plot of proton conductance through V_2O_5 nanochannels with 10^{-4} M HCl.

membrane was measured as a function of relative humidity content in the atmosphere. For the electrical conductivity measurements two copper wires were fixed at both ends of the rectangular strips with dimensions of around 17 mm × 5 mm × 0.028 mm, shown in the inset of Fig. 2e. As can be seen from Fig. 2e, up to 40% RH, the conductivity of the V_2O_5 membrane decreases with the decreasing relative humidity level (RH). However, with further decrease in the humidity level the conductivity started rising again. This peculiar behaviour of atmospheric humidity dependent conductivity is attributed to the formation of interconnected water chains inside the hydrophilic V_2O_5 nanochannels by the water molecules absorbed from the humid atmosphere, which can contribute to the overall conductivity. As the humidity level decreases, the water chains break down resulting in a decrease in the overall conductivity value, also supported by the weight loss data of the membrane as a function of the atmospheric relative humidity level (RH%), shown in ESI Fig. S8.† At 40% RH, all the water chains break down, but localised islands of water molecules remain intercalated inside the V_2O_5 nanochannels. These localised islands of water molecules do not contribute to the overall conductivity but hinder electron transfer between the intercalating sheets. Further decrease in the humidity level, removes these water islands leading to better electrical connection between the lamellar sheets, and hence the conductivity starts rising again. Considering the conductivity of the V_2O_5 membrane at the lowest humidity level as the contribution of electrical conductivity, the proton conductivity was recalculated as 0.01 S cm^{-1}. Remarkably, the conductivity value of V_2O_5 nanofluidic devices, even after deducting electrical contribution, with a 10^{-5} M HCl solution is in the same range as the conductivity values of commercial Nafion membranes with 2 M HCl.[40]

The measured proton conductivity values are a product of the concentration of H^+ ions inside the V_2O_5 nanochannels and their mobility; hence it is important to determine one of these parameters independently. It has been well-accepted that in the surface-charge-governed regime the concentration of H^+ ions inside the nanochannels is determined by the surface charge density (σ_S) of the channel walls. Therefore, σ_S of V_2O_5 nanosheets was first determined by employing the ion-exchange method.[38] At first, all the movable ions of V_2O_5 were exchanged with Li^+ by stirring a strip of dimension 15 mm × 8 mm × 0.022 mm in 10 ml 2 M LiCl aqueous solution for 24 hours, followed by washing with excess water to remove the spare Li^+ ions. The Li^+ ions electrostatically attached to the V_2O_5 sheets were re-exchanged with H^+ by stirring in 10 ml, 1 mM HCl solutions for 24 hours. The number of Li^+ ions exchanged (N_P) with H^+ ions was calculated from the conductivity difference of the supernatant liquid, considering the conductance of HCl and LiCl as 425 S and 115 S, respectively. The surface charge density of V_2O_5 nanosheets was calculated to be 1.13 mC m^{-2} by employing eqn (1).

$$\sigma_S = \frac{N_P \times e}{n \times l \times w} \tag{1}$$

where, n is the number of nanochannels obtained by dividing membrane thickness by the d-spacing of the V_2O_5 strip, e is the elementary charge and l and w represent the length and width of the strip, respectively. Assuming that the number of charge carriers inside the V_2O_5 nanofluidic channels will be equivalent to the number of exchangeable protons (with Li^+ ions) in V_2O_5 nanosheets the proton mobility (μ_+) within the nanochannel was calculated from the conductance (G_S) values in surface-charge-governed regime using eqn (2).[36,39,41]

$$G_S = 2\mu_+\sigma_S\frac{w}{l}. \tag{2}$$

The μ_{H^+} value (5.04×10^{-3} cm^2 V^{-1} s^{-1}) calculated as such was found to be slightly higher than those in the bulk water and commercial Nafion membranes.[42]

In order to verify the values of surface charge density and proton mobility, these parameters were also determined from the transition concentration (C_t), the concentration at which the characteristics of ionic conductivity change from bulk-like to surface charge-governed-like behavior.[41] The C_t values of the V_2O_5 membrane were determined from the intersection of the lines laid over the two distinct conductivity regimes of the conductivity *versus* concentration plot as shown in ESI Fig. S9.† σ_S and C_t are related through eqn (3).[41,43]

$$\sigma_S = \frac{C_t N_A e h_o}{10^{-3}} \tag{3}$$

The σ_S and μ_{H^+} calculated as such (1.4 mC m^{-2} and 4.07×10^{-3} cm^2 V^{-1} s^{-1}, respectively) were found to be in reasonable agreement with the values calculated by the ion-exchange method ($\sigma_S \approx 1.13$ mC m^{-2} and $\mu_{H^+} \approx 5.04 \times 10^{-3}$ cm^2 V^{-1} s^{-1}, respectively).

In order to understand the mechanism of such high proton transport though V_2O_5 nanochannels, the conductivity of a device was measured as a function of temperature with 10^{-4} M HCl solution. As can be seen from ESI Fig. S10,† the conductivity of the devices increases with increasing temperature. From the Arrhenius-plot of ln G *vs.* $1/T$, the activation energy for the proton transport through the nanochannels was calculated to be of 0.066 eV (Fig. 2f). This low value of activation energy suggests that inside the V_2O_5 nanochannels protons follow a Grotthuss-like hopping mechanism,[38,44] where charge is transported by synchronised hopping of H^+ ions between two-dimensionally arranged water molecules within the molecularly thin V_2O_5 nanochannels.

The vanadium pentoxide based nanofluidic devices also demonstrated interesting membrane shape dependent nanofluidic characteristics. As compared to the linear *I–V* curve (shown in Fig. 2b) for a nanofluidic device of a rectangular piece of membrane, the device made from a triangularly cut vanadium pentoxide membrane (Fig. 3a) displayed a non-linear *I–V* curve (shown in Fig. 3b). This behaviour of the non-linear *I–V* curve of the nanofluidic devices is known as Ionic Current Rectification (ICR). ICR occurs because of the preferential direction of ion flow through the nanofluidic channels, due to which current recorded at a certain voltage (+*V*) is different from the one recorded at an equal voltage of opposite polarity (−*V*). Such a controlled and selective flow of ions through biological channels in cell membranes is fundamental to all living cells.[45] ICR has been also demonstrated in artificial systems like conical nanopores,[46,47] longitudinal heterostructured nanotubes,[48] homogeneous nanochannels with asymmetric bath concentrations,[49] triangular membranes of reconstructed graphene oxide sheets[50,51] and heterogeneous MoS_2/WSe_2 bilayered membranes.[52]

The *I–V* curve in Fig. 3b was recorded through an isosceles triangle of a V_2O_5 membrane (18 mm (altitude) × 7 mm (base) × 0.022 mm (thickness)) with an aqueous solution of 10^{-4} M KCl placed on both the reservoirs. The bias was applied at the base side of the triangle. The non-linear *I–V* curve clearly reveals that current through the V_2O_5 triangle at a positive bias is significantly higher than that at a negative bias of similar magnitude. The ICR ratio, calculated as the ratio of the magnitude of the current value at +1 V to −1 V, was found to be 17. Interestingly, when the reservoirs of the same triangular device were filled with 1 M KCl the *I–V* curve became symmetrical (Fig. 3c), implying disappearance of ICR behavior. In Fig. 3d, a plot of the ICR ratio as a function of KCl concentration is shown. In the surface-charge-governed regime (10^{-6} to 10^{-3} M), the high value of the ICR ratio (∼17) was found to be independent of KCl concentrations; however, in the high concentration regime (10^{-3} to 1 M) the ICR ratio decreases with an increase in concentration. The above results suggest that ICR is related to the unipolar conductivity in the surface-charge-governed regime. However, surface-charge-governed conductivity alone does not produce ICR, an asymmetry in the channel geometry is essential. Fig. 4b shows the *I–V* curves recorded through the devices made from the same V_2O_5 membrane with different asymmetry ratios (base (l_b)/tip (l_t) = 3 to 14) (Fig. 4a). It is clearly seen from Fig. 4c that with an increasing degree of geometrical asymmetry the ICR ratio also increased (from 2.5 to 17). The different nature of the ion flow in the opposite

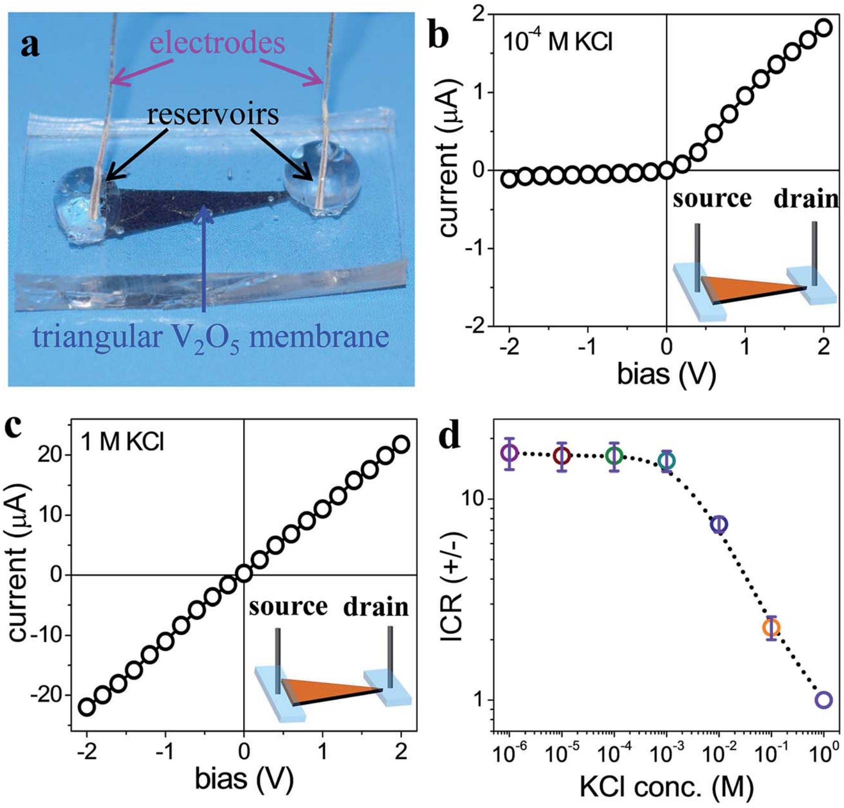

Fig. 3 Ionic current rectification: (a) digital photo showing an isosceles triangular nanofluidic device of V_2O_5. I–V curves of the triangular V_2O_5 device with (b) 10^{-4} M, and (c) 1 M aqueous KCl solution in both the reservoirs. (d) ICR ratio as a function of electrolyte concentration.

direction of the V_2O_5 triangle was also confirmed by measuring ionic current at a constant potential difference for a definite period of time. In Fig. 4d, the open squares (black) and triangles (blue) represents ionic current as a function of time on applying forward (+0.5 V) and reverse (−0.5 V) bias from the base to the tip side of a triangular device ($l_b/l_t = 14$), respectively. The open squares in Fig. 4d clearly show that in the initial stage of bias application, ionic current increases with time, while at the reverse bias it decreases (open triangle), before reaching the steady state. Due to its unique geometry, the magnitude of ionic current through the V_2O_5 triangle is determined by the number of ions moving through the tip. At the forward bias, K^+ ions move from a larger opening, (*i.e.* from the base side) to a smaller exit (*i.e.* to the tip side), so the ionic concentration increases near the tip area. At the reverse bias, ions move from the tip to the base side; here the exit is bigger than the entrance so the ionic concentration is reduced near the tip. The experiment was also repeated after widening the tip of the V_2O_5 triangle ($l_b/l_t = 6$). The open diamond (red) and circle (dark green) curves in Fig. 4d show that the V_2O_5 triangle with $l_b/l_t = 6$ exhibits similar accumulation and depletion behavior, but, the degree of accumulation/depletion decreases with decreasing asymmetry. The accumulation and depletion of the ions flowing in the opposite direction are caused by the geometrical asymmetry of the triangle, and it is possible to tune the degree of accumulation/depletion by tuning the geometry of the triangles. For better comparison purpose, all four curves in Fig. 4d were normalized at the first point of the curve.

A schematic representation of ICR mechanism is shown in Fig. 4e. ICR occurs in the surface charge governed regime, where nanochannels are predominately filled with counter-ions (K^+ ions), by rejecting co-ions (Cl^- ions). In this concentration regime, the concentration of the counter-ions inside the nanochannels is higher than that of the reservoirs. Due to the geometrical restrictions the total current flowing through the V_2O_5 triangle is determined by the number of ions flowing through the tip of the triangle, the region of highest geometrical resistance. At forward bias, K^+ ions flow from the tip of the V_2O_5 triangle to the reservoir, from a region of higher ionic concentration to a reservoir of lower concentration, and hence it produces higher ionic current. The higher concentration of K^+ ions near the tip area originated from the surface charge of V_2O_5 and ion accumulation due to the geometrical asymmetry (Fig. 4e, "forward bias"). Similarly, the lower ionic current at reverse bias is attributed to the ion depletion near the tip area due to the flow of ions from a region of lower ionic concentration (from the reservoir to the V_2O_5 triangle), and also the geometrical restriction (smaller entrance with a bigger exit).

The two-dimensional ion rectifier of V_2O_5 also pumps ions against the concentration gradient under fluctuating external potential with zero mean. As shown in the schematic of Fig. 5a, both the reservoirs of a triangular V_2O_5 device were filled with

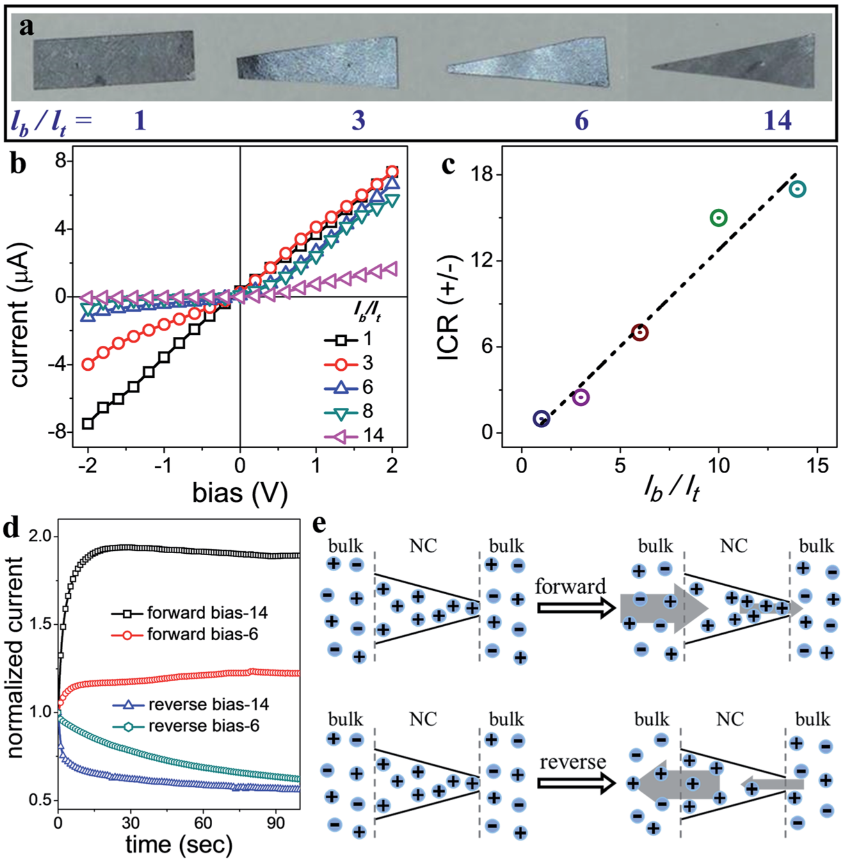

Fig. 4 Mechanism of ICR: (a) photos of vanadium oxide strips with different base (l_b) to tip (l_t) ratios. (b) I–V curves and (c) ICR ratio recorded with V_2O_5 strips of different degrees of asymmetry (l_b/l_t). (d) Plots showing normalized ionic current as a function of time at constant forward (+0.5 V) and reverse (−0.5 V) bias with a V_2O_5 membrane of different asymmetry (l_b/l_t = 14 and 6). (e) Schematic illustration of ICR with 2D triangular nanochannels.

aqueous KCl solution of different concentrations, keeping the concentration of the "base reservoir" fixed at 10^{-5} M, the concentration of the "tip reservoir" was varied from 10^{-5} to 1 M. The electric field between the Ag/AgCl electrodes (source at the base side) was periodically varied between +1 and −1 V, and the current response of the triangular device was recorded as a function of time. As shown in Fig. 5b, for a 1000-fold concentration difference (10^{-2} to 10^{-5} M), a positive average current of 3.4×10^{-7} amp (dotted red line) was observed under the fluctuating electric field with zero mean, suggesting the flow of K^+ ions against the concentration gradient. A similar trend was also observed for 1, 10 and 100 fold concentration gradients, see ESI Fig. S11.† When the concentration difference was enhanced beyond 1000 (for 10^4 and 10^5) the chemical potential of the concentration gradient overtook the ion pumping effect and a mean negative current was recorded, suggesting the flow of ions from higher to lower concentration reservoirs (shown in ESI Fig. S11d† and 5c, respectively). The flowing of ions from lower to higher concentration was also confirmed by measuring the initial and final concentrations of the electrolytes in both the reservoirs. In order to enhance the effect of ion pumping, a device was fabricated by incorporating six triangular membranes, where all the drain and source reservoirs are interconnected. A photo of the same is shown in ESI Fig. S12a.† The current was recorded as a function of time by periodically fluctuating the electric field between +0.5 V and −0.5 V, a potential with zero mean. ESI Fig. S12b† shows the plot of current as function of time for a 10-fold (10^{-2} to 10^{-3} M KCl) concentration gradient. As expected a positive average current (red dotted line) was observed. The initial and final concentrations of both the reservoirs are measured from the slopes of the I–V curves and shown in ESI Fig. S12c and S12d,† source and drain reservoirs, respectively. The difference in the concentrations of ions in the source and drain reservoirs before and after ion pumping are compared in ESI Table S1.† The concentration of ions in the drain side (reservoirs with higher initial ionic concentration) was found to be increasing and that on the source side (reservoirs with lower initial ionic concentration) was found to be decreasing under the fluctuating electric field, confirming the ion pumping effect of the triangular V_2O_5 membrane against the concentration gradient. In order to further confirm the ion pumping effect, I–V curves of the triangular V_2O_5 device were recorded by maintaining concentration gradients between the salt reservoirs. As can be seen from Fig. 5d, the current at positive bias was significantly higher than that at negative bias against the concentration difference

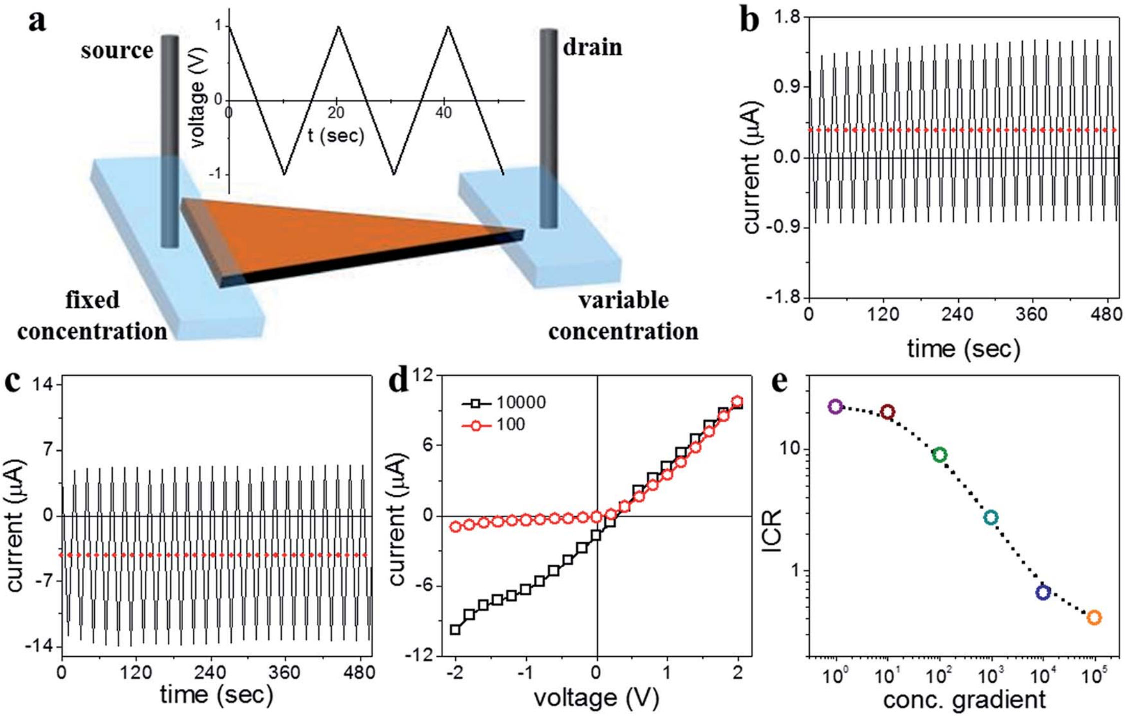

Fig. 5 Ion pumping with a triangular nanofluidic device: (a) schematic representation of the triangular nanofluidic device. Plot of current as a function of time recorded under a fluctuating electric field with zero mean (between +1 V and −1 V) through a V_2O_5 triangular strip with concentration gradients of (b) 10^3 and (c) 10^5. (d) *I*–*V* curves and (e) ICR ratio through the V_2O_5 triangular strip for different concentration gradients. In each of the experiments, the electrolyte in the source reservoir is kept fixed at 10^{-5} M KCl.

of 100 fold (red open circle curve). Fig. 5e shows the ICR as a function of concentration difference revealing that V_2O_5 devices can pump K^+ ions against up to 1000-fold concentration difference, after which the effect of the concentration gradient dominates the net flow of ions.

Conclusion

In conclusion, we have demonstrated that a flexible and free-standing membrane of vanadium pentoxide can be prepared just by re-assembling its exfoliated layers. The atomically thin space between the layers of the vanadium pentoxide membrane was exploited as nanofluidic channels to study ion transport characteristics under extreme confinement. Due to the coordinated hopping of protons between two-dimensionally arranged water molecules, vanadium pentoxide nanofluidic channels exhibit a remarkable proton mobility 5.04×10^{-3} cm^2 V^{-1} s^{-1}, the highest among all the layered materials based nanofluidic devices reported so far. Moreover, vanadium pentoxide based nanofluidic devices exhibit a membrane shape dependent ion transport characteristic. While the rectangular pieces of membranes exhibit linear *I*–*V* curves, the triangularly cut membranes display a diode-like ionic current rectification behavior in the surface-charge-governed regime. The rectification ratio of the vanadium pentoxide triangle can be easily tuned just by tuning its shape. The triangular ion rectifier of V_2O_5 also pumps ions against the concentration gradient under the fluctuating external potential with zero mean. Given the unique optical and electronic properties of vanadium oxide, its molecularly thin nanofluidic channels could offer a new platform for discovering exciting nanofluidic and mixed conducting properties. Additionally, systematic studies on the ion transport characteristic through the interlayer spacings of vanadium oxide would help to understand/improve the performance of vanadium oxides in areas like lithium/sodium ion batteries, chemical sensing, and catalysis.

Conflicts of interest

The authors declare no competing financial interest.

Acknowledgements

K. R. acknowledges the Ramanujan Research Grant (SB/S2/RJN-141/2014) and Start-up Research Grant (Young Scientists) (YSS/2015/000575) of the Science and Engineering Research Board (SERB), India for financial support. All the authors thank CIF-IIT Guwahati for their help with sample characterization. RG, AN, and TK are also grateful to IITG for PhD fellowships.

References

1 G. G. Hammes, *Proc. Natl. Acad. Sci. U. S. A.*, 1982, **79**, 6881.
2 Z. Siwy and A. Fuliński, *Phys. Rev. Lett.*, 2002, **89**, 198103.
3 Z. Siwy and A. Fuliński, *Am. J. Phys.*, 2004, **72**, 567.
4 Y. Zhang and G. C. Schatz, *J. Phys. Chem. C*, 2017, **121**, 161.

5 X. Wu, P. Ramiah Rajasekaran and C. R. Martin, *ACS Nano*, 2016, **10**, 4637.

6 Z. Chen, T. Chen, X. Sun and B. J. Hinds, *Adv. Funct. Mater.*, 2014, **24**, 4317.

7 Y. Zhang, C.-T. Lai, B. J. Hinds and G. C. Schatz, *J. Phys. Chem. C*, 2016, **120**, 14495.

8 L. Wang, Y. Feng, Y. Zhou, M. Jia, G. Wang, W. Guo and L. Jiang, *Chem. Sci.*, 2017, **8**, 4381.

9 N. Bahlawane and D. Lenoble, *Chem. Vap. Deposition*, 2014, **20**, 299.

10 H. Miyazaki, T. Matsuura and T. Ota, *RSC Adv.*, 2017, **7**, 2388.

11 S. Nishio and M. Kakihana, *Chem. Mater.*, 2002, **14**, 3730.

12 S. Kumar, A. Qadir, F. Maury and N. Bahlawane, *ACS Appl. Mater. Interfaces*, 2017, **9**, 21447.

13 C. G. Granqvist, *Phys. Scr.*, 1985, **32**, 401.

14 C. Wu, H. Wei, B. Ning and Y. Xie, *Adv. Mater.*, 2010, **22**, 1972.

15 V. Simic-Milosevic, N. Nilius, H. P. Rust and H. J. Freund, *Phys. Rev. B: Condens. Matter Mater. Phys.*, 2008, **77**, 125112.

16 B. M. Weckhuysen and D. E. Keller, *Catal. Today*, 2003, **78**, 25.

17 B. Saravanakumar, K. K. Purushothaman and G. Muralidharan, *ACS Appl. Mater. Interfaces*, 2012, **4**, 4484.

18 J. Mei, T. Liao, L. Kou and Z. Sun, *Adv. Mater.*, 2017, **29**, 1700176.

19 Y. Li, C. Liu, Z. Xie, J. Yao and G. Cao, *J. Mater. Chem. A*, 2017, **5**, 16590.

20 M. Yan, P. He, Y. Chen, S. Wang, Q. Wei, K. Zhao, X. Xu, Q. An, Y. Shuang, Y. Shao, K. T. Mueller, L. Mai, J. Liu and J. Yang, *Adv. Mater.*, 2018, **30**, 1703725.

21 J. Gao, Y. Feng, W. Guo and L. Jiang, *Chem. Soc. Rev.*, 2017, **46**, 5400.

22 Y. Xu, *Adv. Mater.*, 2018, **30**, 1870019.

23 L. Ding, Y. Wei, L. Li, T. Zhang, H. Wang, J. Xue, L.-X. Ding, S. Wang, J. Caro and Y. Gogotsi, *Nat. Commun.*, 2018, **9**, 155.

24 S. K. Min, W. Y. Kim, Y. Cho and K. S. Kim, *Nat. Nanotechnol.*, 2011, **6**, 162.

25 E. T. Lam, A. Hastie, C. Lin, D. Ehrlich, S. K. Das, M. D. Austin, P. Deshpande, H. Cao, N. Nagarajan, M. Xiao and P.-Y. Kwok, *Nat. Biotechnol.*, 2012, **30**, 771.

26 A. Siria, P. Poncharal, A.-L. Biance, R. Fulcrand, X. Blase, S. T. Purcell and L. Bocquet, *Nature*, 2013, **494**, 455.

27 W. Sparreboom, A. van den Berg and J. C. T. Eijkel, *Nat. Nanotechnol.*, 2009, **4**, 713.

28 C. Yan, C. Lv, Y. Zhu, G. Chen, J. Sun and G. Yu, *Adv. Mater.*, 2017, **29**, 1703909.

29 W. Guo, C. Cheng, Y. Wu, Y. Jiang, J. Gao, D. Li and L. Jiang, *Adv. Mater.*, 2013, **25**, 6064.

30 J. Ji, Q. Kang, Y. Zhou, Y. Feng, X. Chen, J. Yuan, W. Guo, Y. Wei and L. Jiang, *Adv. Funct. Mater.*, 2017, **27**, 1603623.

31 H. Cheng, Y. Zhou, Y. Feng, W. Geng, Q. Liu, W. Guo and L. Jiang, *Adv. Mater.*, 2017, **29**, 1700177.

32 R. B. Darling and S. Iwanaga, *Sadhana*, 2009, **34**, 531.

33 S. Beke, *Thin Solid Films*, 2011, **519**, 1761.

34 Y. Li, J. Yao, E. Uchaker, J. Yang, Y. Huang, M. Zhang and G. Cao, *Adv. Energy Mater.*, 2013, **3**, 1171.

35 M. Giorgetti, S. Passerini, W. H. Smyrl and M. Berrettoni, *Inorg. Chem.*, 2000, **39**, 1514.

36 K. Raidongia and J. Huang, *J. Am. Chem. Soc.*, 2012, **134**, 16528.

37 K. Hatakeyama, M. R. Karim, C. Ogata, H. Tateishi, A. Funatsu, T. Taniguchi, M. Koinuma, S. Hayami and Y. Matsumoto, *Angew. Chem., Int. Ed.*, 2014, **53**, 6997.

38 J.-J. Shao, K. Raidongia, A. R. Koltonow and J. Huang, *Nat. Commun.*, 2015, **6**, 7602.

39 S. Qin, D. Liu, G. Wang, D. Portehault, C. J. Garvey, Y. Gogotsi, W. Lei and Y. Chen, *J. Am. Chem. Soc.*, 2017, **139**, 6314.

40 S. Slade, S. A. Campbell, T. R. Ralph and F. C. Walsh, *J. Electrochem. Soc.*, 2002, **149**, A1556.

41 R. B. Schoch and P. Renaud, *Appl. Phys. Lett.*, 2005, **86**, 253111.

42 P. Knauth, E. Sgreccia, A. Donnadio, M. Casciola and M. L. Di Vona, *J. Electrochem. Soc.*, 2011, **158**, B159.

43 T. J. Konch, R. K. Gogoi, A. Gogoi, K. Saha, J. Deka, K. A. Reddy and K. Raidongia, *Mater. Chem. Front.*, 2018, **2**, 1647–1654.

44 D. D. Ordinario, L. Phan, W. G. Walkup Iv, J.-M. Jocson, E. Karshalev, N. Hüsken and A. A. Gorodetsky, *Nat. Chem.*, 2014, **6**, 596.

45 B. Hille, *Harvey Lect.*, 1988, **82**, 47.

46 J. J. Kasianowicz, E. Brandin, D. Branton and D. W. Deamer, *Proc. Natl. Acad. Sci. U. S. A.*, 1996, **93**, 13770.

47 Z. Siwy, Y. Gu, H. A. Spohr, D. Baur, A. Wolf-Reber, R. Spohr, P. Apel and Y. E. Korchev, *Europhys. Lett.*, 2002, **60**, 349.

48 R. Yan, W. Liang, R. Fan and P. Yang, *Nano Lett.*, 2009, **9**, 3820.

49 L.-J. Cheng and L. J. Guo, *Nano Lett.*, 2007, **7**, 3165.

50 M. Miansari, J. R. Friend and L. Y. Yeo, *Adv. Sci.*, 2015, **2**, 1500062.

51 J. Gao, A. R. Koltonow, K. Raidongia, B. Beckerman, N. Boon, E. Luijten, M. Olvera de la Cruz and J. Huang, *Mater. Chem. Front.*, 2018, **2**, 475.

52 Y. Feng, L. Ding, D. Ji, L. Wang and W. Guo, *Chin. Chem. Lett.*, 2018, **29**, 892.